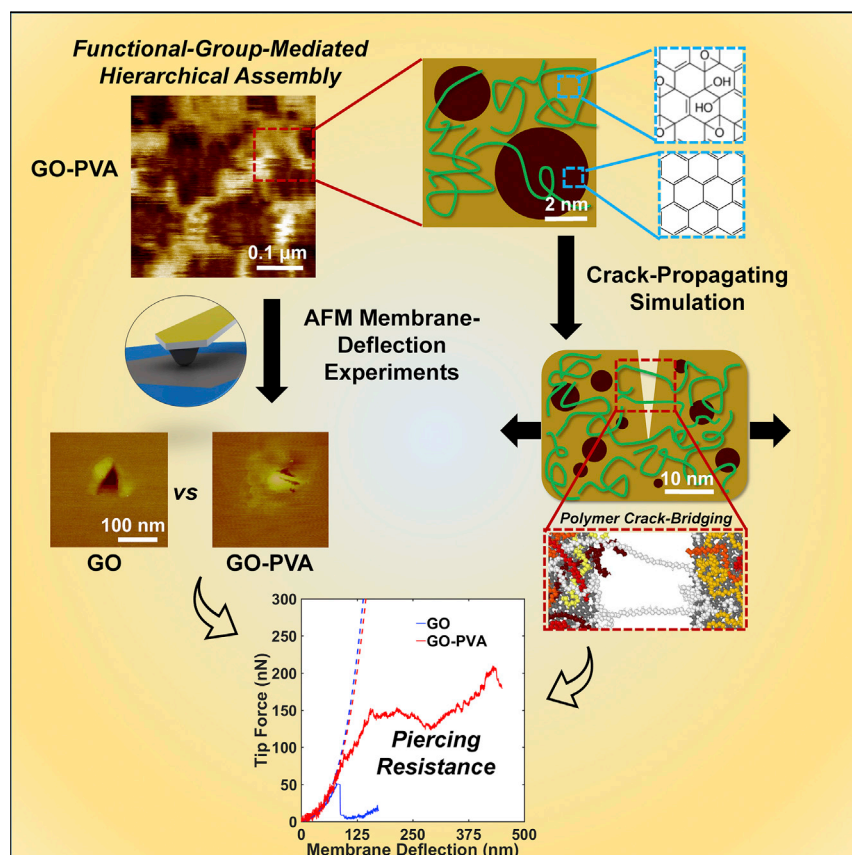


Article

Atomically Thin Polymer Layer Enhances Toughness of Graphene Oxide Monolayers



A bottom-up design and assembly of synergistically interacting graphene oxide (GO)-ultrathin polymer nanolaminates exhibit an impressive 2-fold enhancement in GO toughness and several-fold increase in piercing resistance and load-bearing capacity. This design strategy takes advantage of a hierarchy of interactions between GO and the polymer adlayer, giving rise to an extrinsic toughening mechanism that utilizes the native GO surface chemistry. Such a framework is readily transferable to other 2D material systems to facilitate their adoption in many applications.

Rafael A. Soler-Crespo, Lily Mao, Jianguo Wen, ..., Jiaying Huang, SonBinh T. Nguyen, Horacio D. Espinosa

espinosa@northwestern.edu (H.D.E.)
stn@northwestern.edu (S.T.N.)
jiaying-huang@northwestern.edu (J.H.)

HIGHLIGHTS

GO-polymer nanolaminates with several-fold increase in piercing resistance

Tailored polymer chain length facilitates excellent interdomain reinforcements

Strongly interacting polymer adlayer induces a 2-fold toughness enhancement

Multiscale simulations reveal drastic energy dissipation through crack-bridging

3

Understanding

Dependency and conditional studies on material behavior

Soler-Crespo et al., Matter 1, 369–388
August 7, 2019 © 2019 Elsevier Inc.
<https://doi.org/10.1016/j.matt.2019.04.005>



Article

Atomically Thin Polymer Layer Enhances Toughness of Graphene Oxide Monolayers

Rafael A. Soler-Crespo,^{1,7} Lily Mao,^{2,7} Jianguo Wen,^{3,7} Hoang T. Nguyen,¹ Xu Zhang,¹ Xiaoding Wei,^{4,6} Jiaxing Huang,^{5,*} SonBinh T. Nguyen,^{2,*} and Horacio D. Espinosa^{1,4,8,*}

SUMMARY

During the last decade, two-dimensional (2D) materials have emerged as versatile building blocks for the next generation of engineered materials. However, the intrinsically brittle behavior of 2D materials has thus far delayed their adoption in applications such as sensors and structural materials. Herein, we demonstrate a strategy for toughening graphene oxide (GO) through synergistic interfacial interactions between GO monolayers and ultrathin layers of strongly interacting poly(vinyl alcohol) (PVA). By creating GO-PVA and PVA-GO-PVA nanolaminates, we demonstrate a 2-fold increase in GO toughness, which translates into dramatic increases in energy dissipation and piercing resistance. Atomistic simulations show that this remarkable behavior arises from a polymer chain crack-bridging mechanism, resulting from a synergistic combination of interdomain reinforcements across the GO monolayer and extensive GO-polymer interfacial hydrogen-bonding interactions. The reported findings highlight the potential for achieving engineered 2D materials with superior mechanical properties by incorporating deformation and failure-resistant mechanics arising from tailored chemical interactions between constituents.

INTRODUCTION

Two-dimensional (2D) materials in monolayer or few-layer forms have been used in the design of novel sensors, filtration membranes, and wearable electronic devices. In their multilayer form, nanocomposites of these atomically thin 2D materials can in theory be engineered to exhibit unprecedented combinations of specific stiffness and strength. However, their intrinsic brittle behavior and their associated risk for catastrophic failure^{1–5} have thus far precluded their adoption in practical applications requiring superior mechanical properties.

In the area of nanocomposites (structural materials), lightweight 2D materials can address a high demand for safer and more energy-efficient transportation systems, e.g., in automotive and aeronautical applications. Similarly, the next generation of protective body armor has inspired the search for lightweight materials with exceptional piercing resistance.⁶ Composites based on 2D materials appear to be excellent candidates to address these societal needs. For instance, it has been shown that graphene and graphene oxide-polymer systems have the potential to offer superior performance to Kevlar in body armor applications.^{7–9} Likewise, graphene/Al₂O₃ has been utilized as reinforcing components in lightweight aluminum composites.¹⁰ Unfortunately, the presence of “architectural defects” such as voids and wrinkles found in previously produced 2D materials, in thin-film form, resulted in limited mechanical performance.^{1,4,5,11} This has precluded fundamental understanding of their full potential and their robust implementation in the aforementioned engineering applications.

Progress and Potential

Two-dimensional (2D) materials with unconventional properties have emerged as promising candidates for addressing societal needs for advanced electronic devices and strong lightweight composites. However, their intrinsic brittle behavior and the associated risk for catastrophic failure have thus far limited their adoption. Here, we demonstrate a strategy for extrinsically toughening these materials through engineering the surface chemistry of a graphene oxide ultrathin polymer model system. Our combined experimental and computational explorations reveal a hierarchy of interactions that lead to an impressive 2-fold enhancement in graphene oxide toughness without modulus degradation. Such an extrinsic toughening strategy should be applicable to enhance the failure resistance of a variety of 2D materials, in their pristine state or with surface functionalization, which will in turn inspire the design of next-generation electronics and structural materials.



A strategy to gain fundamental understanding of the potential of 2D materials, in their few-layer or structural-material forms, is to investigate specimens with tailored chemistries and controlled architectures in the form of a few layers so as to avoid stacking defects between sheets (wrinkles, voids) that are typically observed in thicker films. While this strategy has been explored computationally,^{1,12,13} the proposed structures exceed current synthesis capabilities. In contrast, here we present a combined experimental and computational approach, based on graphene oxide (GO)^{11,14} and poly(vinyl alcohol) (PVA), as a model material system, to investigate surface chemistry effects and pathways for improved ductility and fracture of 2D materials. We recently showed that GO manifests nanoscale “intrinsic” toughening behavior arising from its epoxide-rich surface chemistry.^{15–17} However, these short-range effects only delay crack initiation and do not provide crack-bridging mechanisms. In this work, we show that a larger-scale, “extrinsic” toughening mechanism may be incorporated into GO monolayers through surface modification by an ultrathin strongly interacting polymer layer. For example, PVA polymer chains with optimal molecular weights can assemble and interact strongly through hydrogen bonding with the oxidized domains in GO, as proved by Fourier-transform infrared spectroscopy,¹⁸ molecular dynamics (MD) simulations,¹⁹ and mechanical characterizations.^{14,16,19} The extensive hydrogen bonding between the PVA chains and the GO surface consequently mechanically reinforces the whole nanosheet by bridging across these relatively weaker and oxidized domains. This process is analogous to the crack-bridging that arises from relatively short fibers embedded in ceramics,^{20–22} and therefore, one can envision that such an extrinsic toughening mechanism of crack-bridging over scales of tens of nanometers can be exploited to engineer 2D monolayer-based materials with superior toughness.

In this work, we experimentally demonstrate the aforementioned mesoscale crack-bridging and extrinsic toughening behaviors for GO-derived materials. By incorporating an atomically thin layer of PVA polymer onto the surface of a GO nanosheet, we show that the toughness of the resulting GO-PVA nanolaminates is increased beyond that of known 2D monolayers, making them highly attractive as scalable building blocks for the next generation of engineered materials. Multiscale characterization reveals the presence of a hydrogen-bonding network on the surface of GO that can be exploited to reinforce its mechanical integrity via PVA adhesion to the oxidized domains in GO. This pairing results in a synergistic toughening mechanism in which the polymer chains effectively bridge a developing crack and allow the nanolaminate to continue bearing load, as verified by combined nanomechanical experimental and theoretical studies. As cracks develop, clusters of hydrogen bonds between GO and the PVA chains break and reform, which permits PVA to act as a self-healing, load-bearing element. Such a deformation mechanism increases by a few fold the fracture toughness of the underlying GO nanosheet and provides key insights not only for the design of 2D materials-based nanocomposites but also for the engineering of more reliable sensors, filtration membranes, and wearable electronic devices.

RESULTS AND DISCUSSION

Study Overview

GO monolayers modified with a ~1.5-nm-thick layer of PVA (total thickness of ~2.5 nm) were fabricated by sequential Langmuir-Blodgett (LB) deposition of GO and PVA onto a patterned Si substrate (see [Figure 1A](#) and [Experimental Procedures](#)). Nanomechanical testing of freestanding GO-PVA nanolaminates, with an overall thickness of ~2.5 nm, was accomplished through atomic force microscopy (AFM) membrane-deflection experiments. Prior to nanomechanical testing, the polymer

¹Theoretical and Applied Mechanics Program, Northwestern University, 2145 Sheridan Road, Evanston, IL 60208, USA

²Department of Chemistry, Northwestern University, 2145 Sheridan Road, Evanston, IL 60208, USA

³Center for Nanoscale Materials, Argonne National Laboratory, Lemont, IL 60439, USA

⁴Department of Mechanical Engineering, Northwestern University, 2145 Sheridan Road, Evanston, IL 60208, USA

⁵Department of Materials Science and Engineering, Northwestern University, Evanston, IL 60208, USA

⁶Present address: Department of Mechanics and Engineering Science, Peking University, Beijing 100871, China

⁷These authors contributed equally

⁸Lead Contact

*Correspondence:
espinosa@northwestern.edu (H.D.E.),
stn@northwestern.edu (S.T.N.),
jiaying-huang@northwestern.edu (J.H.)

<https://doi.org/10.1016/j.matt.2019.04.005>

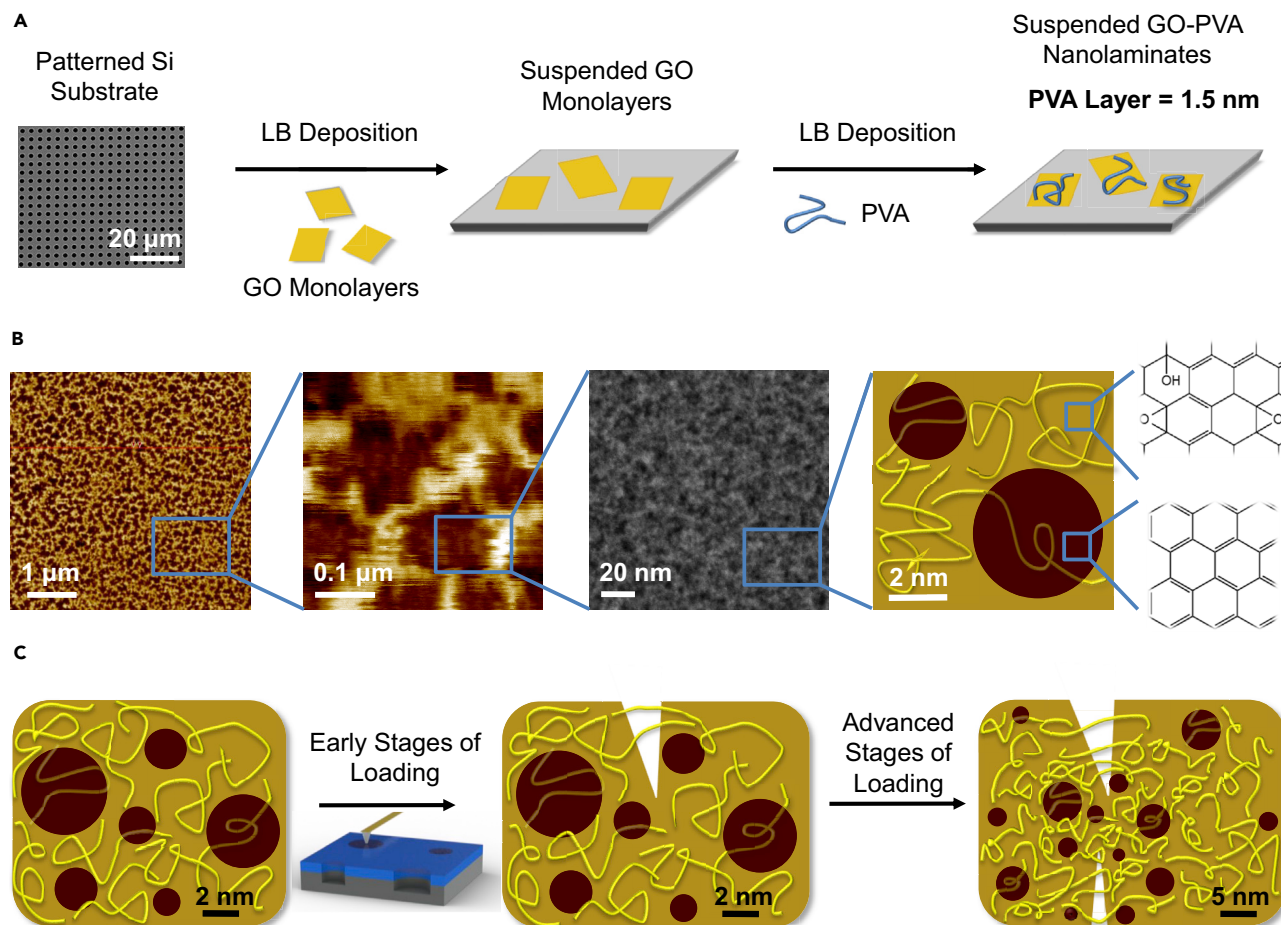


Figure 1. Fabrication, Structure, and Crack-Bridging Mechanism of GO-PVA Nanolaminates

(A) Langmuir-Blodgett fabrication of suspended GO-PVA nanolaminates.

(B) Hierarchical structure of GO-PVA nanolaminates. The AFM images in the first two panels show the microscale structure, and the HAADF image in the third panel reveals the nanoscale structure. The proposed molecular structure based on HRTEM and EELS characterization is shown in the schematic of the fourth panel.

(C) Schematic of the microscale crack-bridging in GO-PVA nanolaminates during AFM membrane-deflection experiments.

In (B) and (C), the brown and gold patches represent graphitic and oxidized domains, respectively, while the yellow fibers denote the PVA chains.

microstructure was studied via AFM (Figure 1B) and the formation of a nanostructured PVA network on GO was confirmed through high-resolution transmission electron microscopy (HRTEM) techniques (Figure 2). Notably, the load-deflection behavior of GO-PVA nanolaminates revealed a 2-fold increase in load-bearing capacity, as compared with unmodified GO monolayers, accompanied by permanent deformation and bulging of PVA in the region where the membranes were loaded (Figure 3). Such deformation and bulging suggest GO cracking accompanied by a polymer “extrinsic toughening” mechanism, schematically shown in Figure 1C. The atomistic basis for this extrinsic toughening mechanism and its quantification was obtained through molecular modeling (Figure 4), in which reformable hydrogen-bonding interactions between GO and PVA chains give rise to a crack-bridging mechanism that results in a significant increase of the load-bearing capacity GO. A continuum-finite element analysis (FEA) (Figure 5) was carried out to estimate the nanolaminate energy dissipation per unit volume and to compare its performance with prior literature reports for the GO-PVA material system.

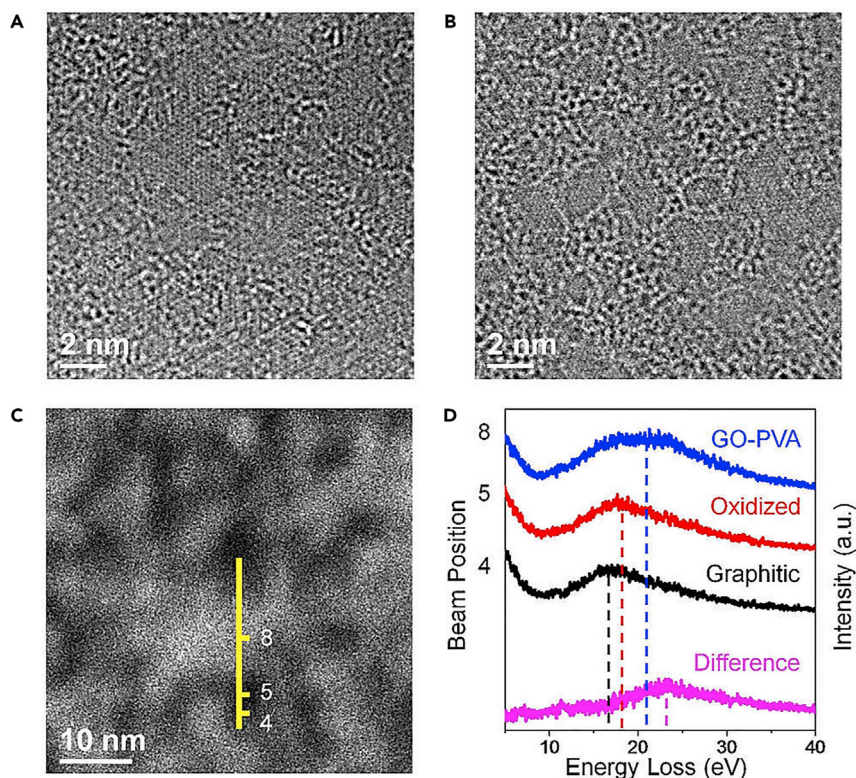


Figure 2. HRTEM and EELS Characterization of GO-PVA Nanolaminates

(A) HRTEM image of a GO nanosheet revealing graphitic islands embedded in a continuous oxidized domain.

(B) HRTEM image of a GO-PVA nanolaminate.

(C) EELS line scan across an HAADF-STEM image of a GO-PVA nanolaminate. The yellow line represents the line-scan pathway, with the numbers corresponding to the beam positions plotted at individual points along the line scan in (D).

(D) EELS spectra corresponding to the line scan in (C). The spectral difference between those for GO-PVA and GO is similar to the EELS signal obtained for a pure PVA sample.

Nanoscale Structure of GO-PVA Nanolaminates

The structure of GO comprised graphitic domains (measuring $\sim 3\text{--}6\text{ nm}^2$) interspersed within a continuous oxidized network.¹¹ Hence, we hypothesize that PVA chains of a suitable length (~ 134 repeat units, 6 kDa molecular weight, and $\sim 33\text{ nm}$ contour length as identified in this study) can optimally interact with, and bridge across, multiple GO oxidized domains due to its comparable size with 3–4 oxidized GO domains and its capability to engage in extensive hydrogen bonding with these domains^{14,16,19} (Figure 1). In contrast, we also hypothesize that longer PVA chains would be less effective in bridging the oxidized domains, as they would preferentially form intramolecular hydrogen bonds, resulting in PVA aggregates on the GO sheet that interact minimally with the oxidized domains. AFM images of nanolaminates fabricated using longer PVA chains ($\sim 140\text{ nm}$ contour length, 25 kDa molecular weight) confirmed that this is indeed the case, showing aggregation of PVA chains into nanoparticles on the GO surface (see [Supplemental Information](#) Section S1 and [Figure S1B](#)). The nanoscale structure of the GO-PVA nanolaminates was examined using HRTEM characterization (see discussion below) and compared with that of GO (Figures 2A and 2B). PVA was not readily distinguishable, since both PVA and the oxidized GO domains are amorphous. To unambiguously detect the presence of PVA, we enlisted electron energy-loss spectroscopy

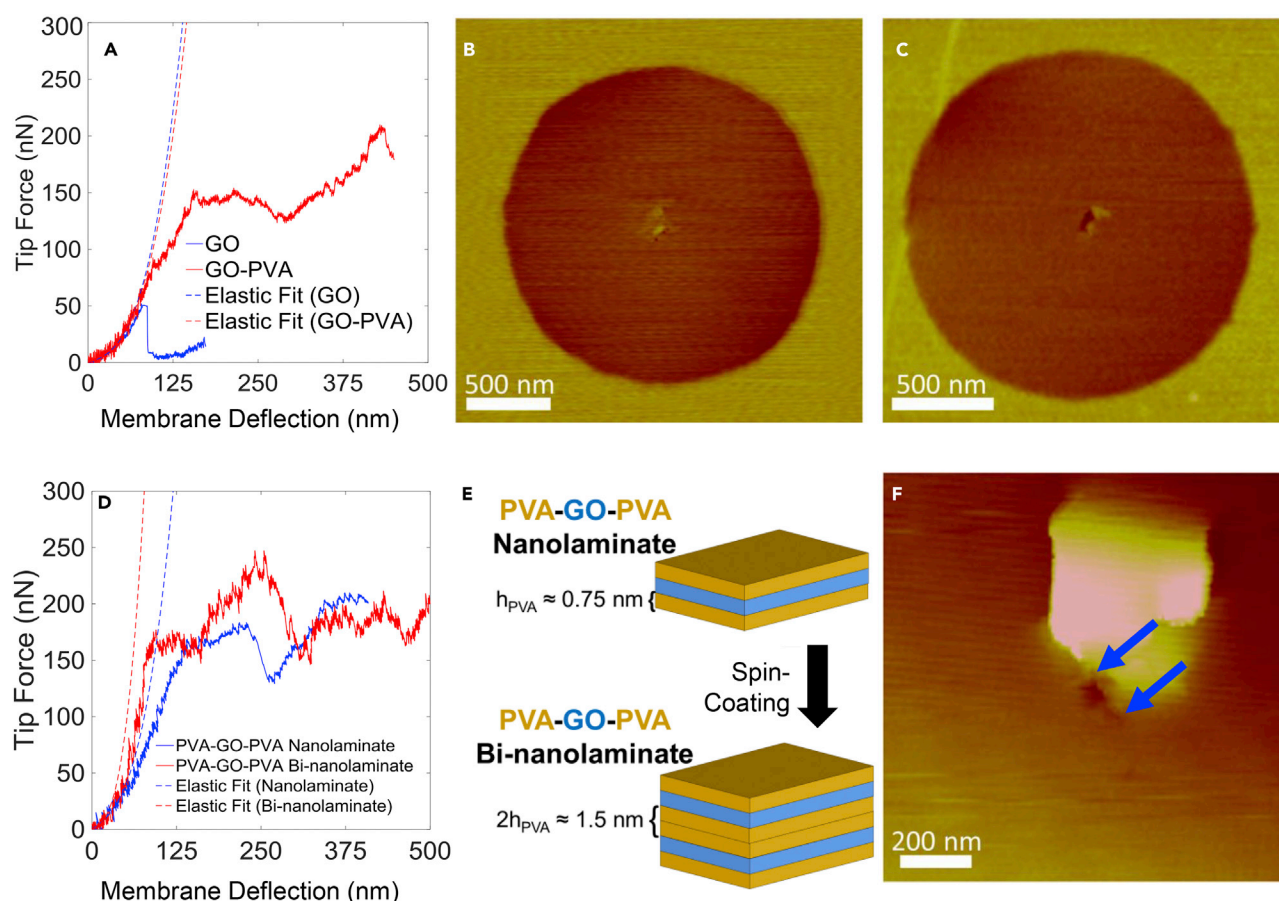


Figure 3. Mechanical Characterization of GO-PVA Nanolaminate Systems

(A) Force-deflection curves for the GO and GO-PVA material systems.

(B and C) Postmortem AFM scan of the membrane surface for (B) GO-PVA and (C) GO.

(D) Force-deflection curves for PVA-GO-PVA nano- and binanolaminates.

(E) Schematic depicting PVA-GO-PVA nanolaminates, obtained by premixing GO and PVA in solution, with PVA thickness h_{PVA} . The thickness of the resulting interface in PVA-GO-PVA nano- and binanolaminates is shown by brackets as a multiple of the thickness of the constituent nanolaminate.

(F) Membrane surface for PVA-GO-PVA binanolaminates. Nanocracks are highlighted by blue arrows. Regions with brighter color represent larger features in the topology, attributable to the bulging of PVA chains near the indented region due to plastic deformations in PVA.

(EELS) to examine spatial variations in the plasmonic peak position of the GO-PVA nanolaminates. We utilized EELS in TEM mode to characterize a series of reference samples to establish peak positions for the graphitic, oxidized, and PVA-covered regions present in GO-PVA nanolaminates (see [Supplemental Information](#) Section S2). The locations of PVA adsorption with respect to the oxidized and graphitic domains of GO were then determined through an EELS line scan in scanning transmission electron microscopy (STEM) mode. This approach exploits the finer lateral resolution of STEM (in our experiments, $\sim 0.25 \text{ nm}$ spot size, compared with a $\sim 500\text{-nm}$ region in TEM). In the high-angle annular dark-field (HAADF) image of the GO-PVA nanolaminate (Figure 2C), an EELS line scan across regions of varying HAADF intensity revealed changes in thickness mass. As the line scan moves from the low-HAADF-intensity region to the high-HAADF-intensity region, across a distance of 10 nm, the $\pi + \sigma$ plasmon peak in the corresponding EELS low-loss spectra shifts from 15 (low-HAADF-intensity) to 17 eV (moderate-HAADF-intensity) and then to 21 eV (high-HAADF-intensity) (Figure 2D). These values correspond to the $\pi + \sigma$ peak positions for graphitic, oxidized, and GO-PVA domains, respectively. In addition,

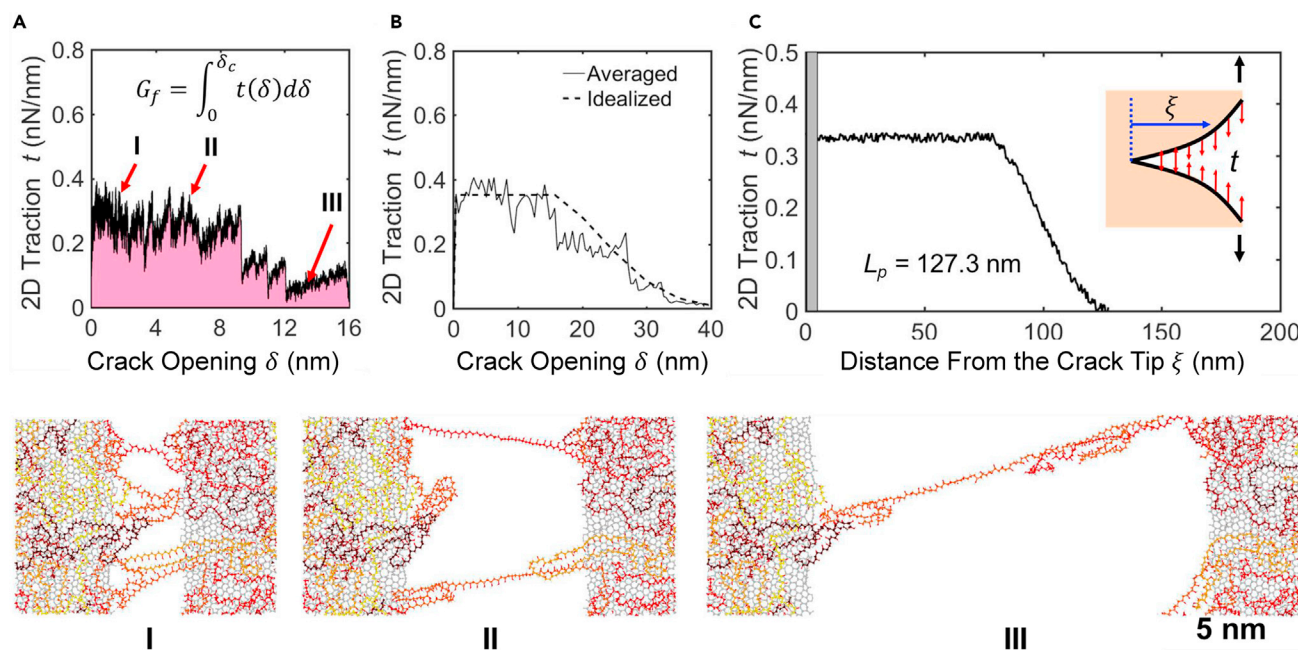


Figure 4. Atomistic and Fracture-Mechanics Analysis of GO-PVA Nanolaminates

(A) Traction-crack-opening behavior of the PVA layer bridging a cracked GO sheet. Labels denote different stages during crack opening, shown in snapshots in the bottom row. The GO substrate was colored in gray, and each PVA chain is assigned different colors for clarity. (B and C) Averaged, over many realizations, and idealized traction-crack opening implemented in the XFEM (B) to estimate the process zone length, L_p , in the single-crack configuration shown in (C). Traction (t) profile in the XFEM calculation as a function of distance from the crack tip (ξ). Inset schematic shows traction-separation contributions (red arrows), which are accounted for in the solid body. GO stresses are modeled explicitly with the PVA traction-crack-opening contribution based on the averaged MD traction-crack-opening result.

subtracting the EELS low-loss spectrum corresponding to the oxidized domain of GO, from the spectrum of GO-PVA, provides the spectral contribution from pure PVA, a peak at 23 eV (Figure 2D). These data suggest that PVA is mostly present on the oxidized domains of the GO sheet (i.e., the continuous high-HAADF-intensity-contrast areas) and confirms the hypothesis that hydrogen-bonding interactions lead to the formation of a nanostructured PVA network on the oxidized domains, which extends over the entire surface of GO (see Supplemental Information Sections S3 and S4).

Interestingly, AFM imaging of the GO-PVA nanolaminates reveals a much larger microscale pattern of interconnected PVA-dense regions (~ 20 – 150 nm in size), consistent with features that arise from polymer density fluctuations (Figure 1B).²³ Similar to the nanoscale dewetting of liquid films on substrates with micron-scale chemical heterogeneities,²³ the heterogeneity of the GO-PVA surface (i.e., graphitic and PVA-covered regions as described above), as revealed by both STEM and AFM, supports that PVA adheres to GO in a scale-dependent fashion (Figures 1A and 1B; Supplemental Information Section S1). The density fluctuations are over a scale that is one to two orders of magnitude larger than the length scale of the chemical heterogeneity, comparable with previous literature.²⁴ Such scale-dependent heterogeneity of polymer adsorption is a reflection of the synergistic interactions between the oxidized domain size of the substrate and a polymer chain of appropriate length (see additional discussion in Supplemental Information Section S1). In contrast, when PVA is deposited on a predominantly graphitic surface, a density fluctuation pattern at the micron scale is not observed by AFM imaging (see Supplemental Information Section S1).

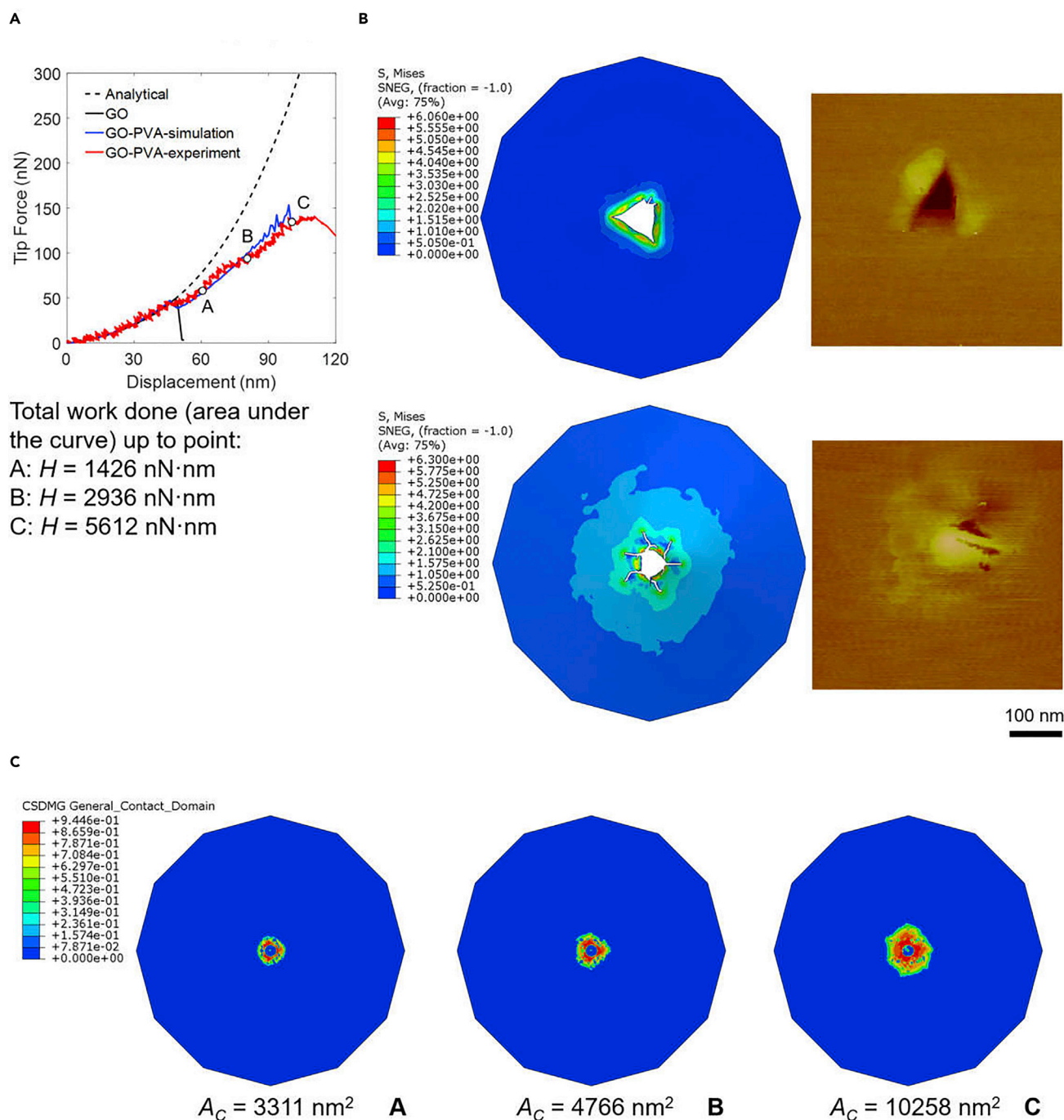


Figure 5. A Comparison between FEA and a Typical Experimental Result (Sample S1)

(A) A good match between simulated and measured force-displacement curves is observed. The simulated work done on the system is also reported at specific points.

(B) Similar shapes and dimensions of punctured holes of the simulated and experimentally GO (top) and GO-PVA membranes (bottom).

(C) Estimations of the inelastic area under the indenter, at increasing loads, from which the energy dissipated per unit volume is computed.

Together, the AFM, HRTEM, and EELS data obtained in this study confirm the presence of a PVA network structure²⁵ composed of nanoscale and microscale features, associated with density fluctuations, which are expected to lead to specific

mechanical behavior. The ultrathin, nanostructured PVA network observed here is evidence of extensive interactions between GO and PVA, which can lead to the bridging of microcracks in the GO, resulting in toughening effects. We hypothesize that this ultrathin PVA layer dominates the mechanical response of the nanolaminates during crack-bridging. As described in the next section, where we carry out nanomechanics experiments to interrogate this behavior, we show that the toughening observed in GO nanolaminates can only arise if PVA chains form continuous networks over oxidized domains that bridge both sides of a crack edge.

Mechanical Performance of GO-PVA Nanolaminates

A typical force-deflection profile of a suspended GO-PVA nanolaminate (Figure 3A) reveals an impressive peak force of approximately 200 nN, a 4-fold increase in the maximum load that monolayer GO can bear before rupture (47 nN).¹⁷ We note that the GO samples in both cases were prepared by the same synthesis method and thus have the same chemical composition and functional group distributions. This superior strength cannot be explained using a rule of mixtures (ROM) model, clearly demonstrating that the PVA chains (strength of 40–140 MPa for bulk PVA^{26–29} versus 25 GPa for GO^{4,16,17}) facilitate the toughening of the GO monolayer. Notably, when the force-deflection profile for GO-PVA nanolaminates (Figure 3A) is fit to a linear elastic membrane solution, over the early stages of deformation (deflection of 25–50 nm), an elastic modulus $E = 78 \pm 11$ GPa is obtained (see Supplemental Information Sections S5 and S8 for in-depth explanations of the ROM predictions and thickness calculation). This value is 2- to 10-fold higher than that of GO-polymer nanocomposites reported in the literature.^{19,26,30–32} which highlights the benefit of utilizing ultrathin polymer layers. Unlike strength, the elastic modulus is in good agreement with ROM predictions, and rapidly approaches the maximum possible value for GO-PVA nanolaminates as the thickness of the PVA layer approaches that of a single chain (~0.5–0.7 nm, as predicted by MD calculations). Together with the increase in rupture force, this reasserts that this ultrathin and nanostructured polymer network provides excellent load transfer and increases energy dissipation and toughness. Indeed, we found that the area under the curve from the membrane-deflection profile increases from 2.5 fJ to ~55 fJ by the addition of a thin PVA layer (see Supplemental Information Section S5).

Given the radius of the AFM tip (~25 nm) and the size of the domains present in GO (Figure 2A), it is reasonable to expect that a large amount of oxidized domains should be present under the region in direct contact with the indenter. Furthermore, given the lower intrinsic strength and fracture toughness of oxidized domains, as compared with graphitic domains,^{5,15,16} we expect that crack initiation and growth will preferentially occur through oxidized domains. Therefore, one can envision that the hydrogen-bond network in the GO-PVA nanolaminates leads to a synergistic redistribution of mechanical loads.³¹ As flaws nucleate in the relatively weaker, oxidized domains of GO, PVA chains bridge these domains (discussed below) during crack opening, enabling microscale crack-bridging mechanisms and toughening GO (manifested as an increased load-bearing capacity). The effects of crack-bridging are apparent in the large nonlinear work-hardening response of the GO-PVA nanolaminates (Figure 3A), and GO-PVA membranes, as previously stated, exhibiting a 20-fold increase in energy absorption compared with pristine GO membranes (see Supplemental Information Section S5). We also show below, in the discussion on the atomistic and finite element modeling of the fracture process, that such behavior is only possible if the reinforcing nanostructured PVA network limits crack growth during the loading process (Figure 1C). If the crack length is comparable with the bridging-zone length (on the order of

the contour length of an adsorbed PVA chain), it is possible to shield the developing flaw and limit its growth.²⁰ Indeed, the rupture of the indented GO-PVA nanolaminate (Figure 3B) is confined to the area in direct contact with the AFM tip (~25 nm radius). This observation is in stark contrast to the more-prominent rupture typically observed for a single GO monolayer (Figure 3C), suggesting that mechanical energy is well dissipated during crack growth. Such a phenomenon can be considered the “nanoscale” version of crack-bridging mechanisms exhibited by fiber-reinforced ceramics and concretes,^{20–22,33} and can provide a pathway to increase the toughness of GO-based and other 2D materials.

Atomistic Basis of Crack-Bridging and Quantification of Energy Dissipation

To obtain atomistic insight into the GO-PVA crack-bridging mechanism and quantify the level of extrinsic toughening, we carried out MD simulations on a representative GO-PVA system to extract fundamental properties and constitutive relationships. We investigated the crack-bridging behavior at the scale characterized by STEM by probing the interfacial load bearing between GO and PVA in the wake of a crack. The interfacial load bearing as a function of crack opening was quantified by monitoring the evolution of traction, i.e., stress on PVA chains due to motion of GO surfaces, with crack opening. Our analysis focuses on GO’s oxidized domains, which are dominant in the microstructure of the material and control the behavior of the system given their hydrogen-bonded interactions with PVA chains. We conducted all-atom MD simulations (see [Experimental Procedures](#) for simulation details) using the ReaxFF force field,³⁴ which has been parametrized³⁵ for hydrocarbons and GO-based systems. In these simulations, PVA chains (134 monomers, ~33 nm contour length) were assembled over two GO sheets with an initial crack opening of 1 nm, and the sheets were then pulled apart to increase the opening of the crack while the 2D traction-crack-opening response of PVA was measured. The 2D traction was computed by dividing the PVA bridging force by the crack length. We note that a complete atomistic simulation of the indentation and crack-propagation process for GO-PVA nanolaminates, which can capture the laboratory length and time scales, is unfeasible due to its prohibitive computational costs.

Mechanistically, the presence of hydrogen-bond clusters between GO and PVA effectively “anchors” PVA chains, enables load bearing across the GO-PVA interface, and becomes responsible for the stretching of PVA chains as cracks in GO propagate. In the early stages of crack opening (i.e., as the two GO sheets are pulled apart), the average traction (Figure 4A) is approximately constant as PVA chains extend over the crack by uncoiling and stretching (Figure 4A, snapshot I). The traction-separation plot exhibits a number of oscillations associated with the breaking and reformation of hydrogen-bond clusters (Figure 4A). The process is repeated over the ensemble of PVA chains during sliding. Finally, as PVA chains are successively pulled out from either GO sheet (Figure 4A, snapshot III), they become progressively unable to bridge the relatively long gaps associated with the GO crack, which leads to a decrease in traction. This mechanism of PVA load transfer to the GO sheets, via networks of hydrogen bonds, causes stretching of the PVA backbone, which greatly enhances the crack-bridging effect. We also found that the load-bearing capability of PVA is strongly dependent on the initial configuration of the polymer, and other mechanisms (e.g., bundling of PVA chains, bridging between interconnected PVA chains) were found to contribute significantly to load bearing (see [Supplemental Information](#) Section S7 for further details). To account for these statistical variations, we repeated simulations on replicas and averaged the 2D traction-crack-opening response for the subsequent fracture mechanics analysis, shown in Figure 4B.

To quantify the increase in toughness, we incorporated the traction-crack-opening behavior captured from the atomistic simulations of GO-PVA nanolaminates in a fracture mechanics framework²⁰ to estimate the energy-release rate involved during crack opening (see [Experimental Procedures](#) for further details). Our analysis reveals that the energy-release rate G of GO-PVA, which arises as the sum of the energy-release rates of GO and the extrinsic PVA crack-bridging, G_0 and G_t , respectively, is on average 11.67 nJ m^{-1} (see [Supplemental Information](#) Section S7). In contrast, single GO monolayers¹⁵ have an intrinsic toughness of $G_0 = 3.4\text{--}4.6 \text{ nJ m}^{-1}$ (for comparison, the intrinsic toughness of graphene is 5.3 nJ m^{-1} ,^{5,15} comparable with GO and lower than GO-PVA nanolaminates). Here, we have normalized the energy-release rates with respect to the number of monolayers (via thickness) to allow comparisons between different systems. We also estimated, employing extended finite element analysis, the process zone length (L_p) for the GO-PVA system, i.e., the region around the GO crack tip with non-zero traction (see [Figures 4B and 4C](#) and [Experimental Procedures](#) for details). The cohesive law, extracted from the all-atom MD, is applied to represent the traction-separation law of the crack. After the crack propagates to a certain length, a steady-state process zone develops that corresponds to $L_p \sim 127 \text{ nm}$. This is in stark contrast to that of quasi-brittle GO, which is approximately 2.5 nm long. In this light, our observations reveal the importance of interfacial load transfer behind the crack tip, provided by PVA chains, via high-density, breakable-and-reformable hydrogen-bond networks, and show the GO-PVA system to be the molecular analog of ceramics reinforced by relatively short fibers.²⁰

High stresses experienced by the material under the indenter initiate failure in the GO-PVA nanolaminates in the form of microcracks,¹⁷ leading to nonlinearities in load-deflection curves. However, in contrast to pristine GO, these microcracks are bridged by PVA chains, delaying microcrack coalescence and failure, which leads to increased toughness. To quantify the gains associated with using GO-PVA in nanolaminates, we carried out FEA of the AFM experiments using the constitutive behavior described in Section S9 of [Supplemental Information](#). [Figure 5A](#) shows a comparison between the FEA simulation and one representative experimental result. The load-displacement behavior up to the peak load of both curves and damage patterns on the membrane are very similar. The dimension of the punctured hole in the GO membrane and GO-PVA are also in excellent agreement with the experimental results as shown in [Figure 5B](#). Due to the presence of the ultrathin PVA layer in the latter case, the cracks are more diffused and a larger area of the GO membrane is resisting the puncture load. It should be noted that the key requirements for this mechanism to occur are: (1) the length (or molecular weight) of the PVA chains are short enough such that most of the chains are well adsorbed onto the oxidized patches ([Supplemental Information](#) and [Figure S4](#)), (2) the chains must be long enough to avoid easy pullout, and (3) the stiffness and covalent strength of the backbone must be exploited to avoid deformation localization under the penetrating tip. These three conditions allow an ultrathin layer of polymer to be both strong (arising from the backbone of polymer chains) and tough (as hydrogen bonds can break and reform during sliding events between GO and PVA). A supplementary condition, which remains a hypothesis, is that under the indenter pressure, PVA chains may organize and heavily crosslink with one another to form a stronger polymer network.

To compare our membrane-deflection results to the stress-strain curves reported in the literature for GO-polymers, which were obtained either experimentally or computationally via MD, we normalized the amount of energy dissipated in the nanolaminate through a unit volume defined by $G_v = H/A_c t$, where H is the

cumulative energy up to a considered state, computed via trapezoidal integration of force-deflection signatures (Figure 5A), A_c is the inelastic area (where the sliding between GO and PVA has occurred, see Figure 5C), and t is the thickness of the nanolaminate system. Values of energy dissipated per unit volume, G_v at points A, B, and C are 0.431, 0.547, and 0.616, respectively. Compared with values reported in the literature for GO-PVA (0.345³⁶ and 0.4,¹⁹ calculated from the area under the stress-strain curves), the estimates of energy dissipated in the membrane-deflection experiments reported herein represent a 2-fold increase.

Mechanical Characterization of PVA-GO-PVA Nanolaminates and Binanolaminates

The crack-bridging mechanism observed for the GO-PVA nanolaminates investigated here suggests that depositing PVA on both faces of the GO monolayer should lead to further improvements in performance, without affecting stiffness, if the polymer volume fraction is kept constant. Such PVA-GO-PVA nanolaminates were prepared by spin-coating a premixed GO-PVA solution³⁷ on a patterned substrate (additional information is provided in [Experimental Procedures](#)). Remarkably, this method enabled thickness reduction of the polymer layer to a single-chain thickness, as AFM imaging indicates that both sides of the GO monolayer are covered by a PVA monolayer with thickness of only ~ 0.75 nm (total sample thickness = 2.5 nm; see [Supplemental Information](#) Section S8). Interestingly, the force-deflection profile of the PVA-GO-PVA nanolaminate (Figure 3D) shows a rupture force of 176 ± 24 nN, a 15% increase with respect to that of GO-PVA nanolaminates (155 ± 31 nN). As anticipated, and since the volume fraction of PVA in the system remains constant, the elastic modulus ($E = 78 \pm 10$ GPa) of the PVA-GO-PVA nanolaminates remains unchanged from that of GO-PVA ($E = 78 \pm 11$ GPa, see [Supplemental Information](#) Section S5).

The success in extending the crack-bridging mechanism to PVA-GO-PVA nanolaminates prompted us to explore whether such toughening behavior can still be observed in stacked assemblies of PVA-GO-PVA nanolaminates, such as a PVA-GO-PVA binanolaminate system. Through spin-coating, we obtained a mix of nanolaminates and binanolaminates on the patterned Si substrate. The 5-nm thickness of the latter is consistent with the stacking of two PVA-GO-PVA nanolaminates of 2.5 nm thickness (see Figure 3E). The 2D elastic modulus of binanolaminate PVA-GO-PVA ($E_{2D} = 365 \pm 72$ N m⁻¹) scales with the number of PVA-GO-PVA nanolaminates ($E_{2D} = 196 \pm 26$ N m⁻¹; see Figure 3D and [Supplemental Information](#) Section S5), confirming the presence of a secondary load-bearing GO layer and suggesting that there is excellent load transfer and contact between adjacent PVA-GO-PVA nanolaminates. This implies that GO-based nanocomposite materials with superior load-carrying and energy-dissipation (area under the load-deflection curve) capacities may be obtained by stacking PVA-GO-PVA nanolaminates, as the mechanical properties of individual PVA-GO-PVA nanolaminates are maintained and load transfer is reasonable.

Consistent with interlaminar load transfer, a peak force of 201 ± 53 nN was measured for PVA-GO-PVA binanolaminates. This increase in peak force over that of the PVA-GO-PVA nanolaminates (176 ± 24 nN) is but one feature of the improved material performance of the binanolaminates. Force-deflection curves and AFM surface analysis suggest that this material is also capable of a large amount of energy dissipation. Indeed, the post-test surface of PVA-GO-PVA binanolaminates distinctly contains a heightened feature, presumably an accumulation of plastically deformed PVA chains (e.g., the bulging of the loaded polymer region), in the center of the membrane after

significant loading followed by unloading. Closer inspection of this feature (Figure 3F) reveals the presence of surrounding nanocracks (~75–100 nm), which do not appear to penetrate through the entire thickness of the binanolaminate assembly. Based on these observations, we hypothesize that this peak force corresponds to the puncture of the top PVA-GO-PVA nanolaminate, which explains why no force scaling is observed. It also suggests the presence of a crack-arrest mechanism—a highly desirable feature in the design of nanocomposites.^{38–40} Indeed, the existence of a large process zone that redistributes load between GO and PVA disrupts the typical failure mechanism of GO. As shown in the force-membrane-deflection curves, (PVA-GO-PVA) nano- and binanolaminates have a significant peak-load enhancement and nonlinear response attributable to the load transfer between GO and PVA chains through the interface. As the membrane is continuously loaded, material nonlinearities lead to load redistribution that delays failure of the top layer. Under sufficiently high applied forces (beyond those used in these experiments, which were limited by the stiffness of the employed cantilever), we would expect to see full binanolaminate failure across the thickness, with distinctive topographical features owing to the load transfer between the two adjacent layers.

Conclusion

As stated in the [Introduction](#), there is a major need for the design and synthesis of new 2D materials exhibiting superior specific stiffness, strength, and toughness. In this regard, the fundamental studies of the mechanics of nanolaminates described in this paper provide key understandings of the pathways for their toughening and explain recent experimental findings hinting at the potential of 2D materials in transportation and ballistic-protection applications.⁹ Indeed, the ultrathin GO-PVA structures reported here show significant failure resistance while preserving good stiffness and light weight. The GO monolayers are significantly toughened by atomically thin layers of PVA through controlled interfacial interactions: the microscale cracks are bridged by the PVA chains, which delay and shield crack growth through a hydrogen-bond-mediated network. Such a mechanism is the molecular analog of macroscopic crack-bridging observed in ceramic- and fiber-reinforced composites. Our fabrication strategy should be applicable to a variety of 2D materials, in their pristine state or with surface functionalization, for enhancing their mechanical performance toward controlling deformation and failure, which, in turn, can inspire the design of the next generation of engineered structural materials.

To fully exploit the findings reported in this paper as they relate to the design of nanocomposites, we must consider three elements. The first is the making of GO with larger sheet dimensions as well as GO-polymer laminates with larger thickness. These are manufacturing challenges that need further exploration. A possible direction is the use of chemical vapor deposition to grow graphene, over the scale of full wafers,⁴¹ followed by oxidation, for instance using plasma treatments with suitable chemistries. Thicker laminates can then potentially be made from this large-dimension GO using scale-up technologies such as roll-to-roll manufacturing⁴² or flow-assisted assembly.⁴³ The second approach is polymer selection and tailoring of the interface chemistry, to modulate crosslinking strength and density via hydrogen bonding, electrostatics, and van der Waals interactions. The ultimate goal is to control the shear strength of the interface while maintaining its ductility.⁴⁴ The third method deals with optimizing the mechanics of the nanocomposite by accounting for the competition between constituent dimensions, interface strength, and GO-sheet properties including toughness. By exploring these variables using shear-lag analytical frameworks,^{45,46} Monte Carlo type simulations,⁴⁷ or analytical frameworks,^{48,49} many novel materials can be designed.

We emphasize that the work reported herein focused on achieving the thinnest polymer layer film that can provide intra- and interlayer load transfer to link sliding layers and simultaneously bridge nanocracks in the GO. While such an approach maximizes the volume fraction of the 2D material, the thickness of the polymer layer is a variable that can be tuned within the structural materials' design space. Given the well-known thickness-dependence of polymer structures and mechanical properties, the response of the GO-polymer nanocomposites can then be tailored⁵⁰ to match a particular performance requirement. In this respect, Gao et al.⁵¹ have recently explored the tradeoff between inter- and intralayer load-bearing mechanisms in graphene-derived layer-by-layer-assembled materials. A similar study for the GO-polymer system could be a topic of future research work. We close by noting that we have laid out methodologies that can be exploited by the scientific community at large in the design and validation of next-generation 2D materials that can meet future needs in applications ranging from sensors to wearable electronic devices to structural materials.

EXPERIMENTAL PROCEDURES

Materials and Instrumentation

Unless otherwise stated, all reagents were used as received. Graphite powder (grade 2139) was purchased from Asbury Carbons (Asbury, NJ). Sodium nitrate, potassium permanganate, absolute ethanol, and concentrated hydrochloric acid were purchased from Sigma-Aldrich (Milwaukee, WI). Concentrated sulfuric acid, ether, and methanol were purchased from VWR International (Radnor, PA). Phosphoric acid (85 wt %), was purchased from Mallinckrodt Baker (Phillipsburg, NJ). Hydrogen peroxide (30 wt % in water) was purchased from Sigma-Aldrich and refrigerated during storage. Ultrapure deionized water (resistivity 18.2 M Ω cm) was obtained from a Milli-Q Biocel A10 system (Millipore, Billerica, MA). Silicon wafers (item #785, 100 mm diameter, p-type, B-doped, single-side-polished) and silicon wafers with a 500-nm-thick thermal oxide layer (100 mm diameter, N/Phos-doped, single-side-polished) were purchased from University Wafer (Boston, MA).

HRTEM, STEM, and EELS characterizations were conducted using the Argonne Chromatic Aberration-corrected TEM (ACAT) (an FEI Titan 80-300 ST with an image aberration corrector to compensate for both spherical and chromatic aberrations) at an accelerating voltage of 80 kV to reduce knock-on damage. The nanolaminate TEM specimens were prepared by sequential LB deposition of GO and PVA, or spin-coating a premixed aqueous solution of GO and PVA, onto TEM grids (see procedures below). HRTEM images were taken under conditions when spherical and chromatic aberration coefficients are corrected below certain values ($C_s < 5 \mu\text{m}$, $C_c < 5 \mu\text{m}$). Low-loss EELS spectra were recorded in an image-coupled mode. To avoid electron beam damage, we used a low probe current (5 pA) in STEM mode, relatively large probe size ($\sim 0.25 \text{ nm}$), and short dwell time (0.1 s) for the EELS line scan.

Scanning electron microscopy (SEM) images were taken using an FEI NovaNano 600 scanning electron microscope (FEI, Hillsboro, OR). CHN elemental analysis and O elemental analysis were performed by combustion and pyrolysis, respectively (Micro Analysis, Wilmington, DE). Samples were dried at 80°C under vacuum for 4 h. Water content was measured by Karl Fischer titration using a C20 Compact Karl Fischer Coulometer (Mettler-Toledo International, Columbus, OH) on films dried at 80°C under vacuum for 4 h, and bath sonicated for 5 min in dry methanol in a sealed vial. Water-contact angles were measured using a VCA Optima contact angle instrument (AST Products, Billerica, MA) by dropping 4 μL of ultrapure deionized water

onto the substrate, with measurements taken at three different locations on each substrate.

Synthesis of Graphene Oxide

Each batch of graphite oxide was prepared using a modified Hummer's method.⁵² In brief, a 9:1 (v/v) mixture of concentrated H₂SO₄ (360 mL)/H₃PO₄ (40 mL) was added to a mixture of graphite (3 g) and potassium permanganate (18 g). The reaction mixture was heated to 50°C and stirred for 12 h. The mixture was then cooled to room temperature and poured over ice (~400 mL), followed by the addition of H₂O₂ (8 mL of a 30 wt % solution) until the solution turned bright yellow. The resulting graphite oxide was filtered through a 250-μm US Standard testing sieve (VWR International) and centrifuged (8,228 relative centrifugal force [rcf] for 1 h) in a model 5804R centrifuge (Eppendorf, Westbury, NY) with the supernatant decanted away. The remaining solid was then washed with ultrapure deionized water (200 mL), HCl (200 mL of a 30 wt % solution), and ethanol (2 × 200 mL). After each wash, the mixture was filtered through the sieve and then centrifuged (8,228 rcf for 1 h) with the supernatant decanted away. The remaining material was coagulated with ether (200 mL) and filtered over a polytetrafluoroethylene membrane (Omnipore, 5 μm pore size; Millipore) overnight. The GO filter cake was then dispersed in ultrapure deionized water, with the dispersion stirred for 18 h. Any residual unexfoliated graphite oxide was removed by centrifuging at 8,228 rcf for 5 min (2×) with the precipitate discarded. The final dispersions contained ~3 mg mL⁻¹ of graphene oxide (GO), with a C/O ratio determined by elemental analysis to be 1.13. Accounting for a water content of 14.53%¹⁷ results in a C/O ratio of 1.57. GO films for analysis were prepared by drop casting GO solution onto silicon wafers with a thermal oxide layer, followed by drying under ambient conditions.

Preparation of Si Substrates with Microwells

Si substrates containing arrays of microwells with 1.76 μm diameter and 4 μm depth were fabricated using a combination of photolithography and deep reactive-ion etching (DRIE). A 1.2-μm-thick photoresist layer (S1813 positive photoresist manufactured by Dow Electronic Materials Microposit, catalog number DEM-10018348; Capitol Scientific, Austin, TX) was spin-coated onto the Si wafer at 4,000 rpm using a spin-coater (Cee 200X; Brewer Science, Rolla, MO). Following a 1-min soft bake at 100°C on a hot plate, the wafer was exposed to UV light (365 nm, 18 mW cm⁻²) for 4 s on a Mask Aligner instrument (Süss MABA6; Süss MicroTec, Garching, Germany). After exposure, the wafer was developed in an MF 319 developer (manufactured by Dow Electronic Materials Microposit, catalog number DEM-10018042; Capitol Scientific) for 60 s. Spin-rinsing was carried out with ultrapure deionized water (200 mL) for 30 s at approximately 300 rpm, followed by a 60 s spin dry at 3,000 rpm.

The resulting photoresist-masked silicon wafer was then subjected to microwell etching using a DRIE machine (STS LpX Pegasus; SPTS Technologies, San Jose, CA). After etching, the remaining photoresist was removed using acetone, and the wafer was cleaned using isopropanol and ultrapure deionized water. This wafer was then cleaved into smaller substrates to be used in the LB deposition and subsequent membrane-deflection experiments.

Prior to LB deposition, the substrates were cleaned using the following procedure: (1) submerged in a 3:1 (v/v) mixture of concentrated H₂SO₄/30 wt % H₂O₂ (2 mL) and heated in a Biotage (Uppsala, Sweden) SPX microwave reactor (software version 2.3, build 6250) at 180°C for 45 min; (2) sonicated for 10 min each in ultrapure deionized water (~10 mL), methanol (~10 mL), and ultrapure deionized water (~10 mL),

respectively; (3) dried under a flow of nitrogen for 1 min; and (4) treated with O₂ plasma (5 min at 190 W and 10–15 mTorr O₂) in a South Bay Technology (San Clemente, CA) Model PC-2000 plasma cleaner. After this cleaning process, the substrates were left under ambient conditions and their water-contact angle was monitored until the desired value was reached prior to LB deposition (see procedure below). As reported previously,¹⁷ the yield of intact suspended GO membranes is dependent on the water-contact angle of the substrate. As such, substrates with a water-contact angle of approximately 60°–70° were used to prevent membrane rupture.

Langmuir-Blodgett Assembly of GO-PVA Nanolaminates

To prepare suspended, single GO monolayers for the AFM membrane-deflection experiments with GO-PVA nanolaminates, we employed the LB assembly method.⁵³ The as-prepared aqueous GO dispersion was diluted with methanol to a mixture of 5:1 (v/v) MeOH/GO dispersion. The Nima Technology (Espoo, Finland) model 116 trough was cleaned with acetone and filled with ultrapure deionized water. Typically, the GO/methanol solution (300–480 μ L) was spread onto the water surface dropwise at a rate of 100 μ L min^{−1} using a glass syringe, forming a monolayer film on the surface. The surface pressure was monitored using a tensiometer attached to a Wilhelmy plate. The film was allowed to equilibrate for at least 20 min after spreading and was then compressed by barriers at a speed of 100 cm² min^{−1}. Single GO monolayers were transferred near the onset of the surface pressure increase by vertically dipping the substrate into the trough and slowly pulling it up at a rate of 2 mm min^{−1}.

The LB technique was also used to deposit an ultrathin PVA layer onto the suspended GO monolayers. To prevent the GO monolayer from washing off during the deposition, we deposited PVA on the day after LB deposition of the GO. A 1 mg mL^{−1} aqueous solution of PVA was diluted with ethanol to a mixture of 5:1 (v/v) ethanol/ultrapure deionized water. (This concentration of the PVA spreading solution is experimentally chosen so that a uniform monolayer coverage on the water surface can be conveniently obtained with a small volume of spreading solution. The actual concentration of PVA on the water surface is solely controlled by the surface pressure upon the transfer.) The Nima Technology model 116 trough was cleaned with acetone and filled with ultrapure deionized water. PVA solution (600 μ L) was spread onto the water surface dropwise at a rate of 100 μ L min^{−1} using a glass syringe, forming a film on the surface. The surface pressure was monitored using a tensiometer attached to a Wilhelmy plate. The film was allowed to equilibrate for at least 20 min after the spreading and was then compressed by barriers at a speed of 100 cm² min^{−1}. The PVA layer was transferred at a surface area of 50 cm² by vertically dipping a substrate containing suspended GO monolayers into the trough and slowly pulling it up at a rate of 2 mm min^{−1}.

Fabrication of PVA-GO-PVA Nanolaminates and Binanolaminates

An aqueous PVA solution was prepared by dissolving PVA (200 mg) in ultrapure deionized water (16.7 mL) and stirring for at least 3 h. This solution was mixed with the as-prepared aqueous GO dispersion (3.335 mL) to yield a 1:20 (w/w) GO/PVA dispersion, which was diluted to a final volume of 30 mL and centrifuged at 8,228 rcf for 20 min. The supernatant was decanted to remove excess PVA not bound to GO monolayers and the precipitate was redispersed in ~27 mL of ultrapure deionized water. The resulting dispersion of PVA-GO-PVA was spin-coated onto the patterned Si substrates at 2,000 rpm, with an acceleration of 200 rpm to obtain a mix of PVA-GO-PVA nano- and binanolaminates, which could be distinguished based on SEM and AFM characterization.

Atomic Force Microscopy Membrane-Deflection Tests

A single-crystal diamond probe (catalog number ART D160; K-TEK Nanotechnology, Wilsonville, OR) was used to load the membrane at its center using an atomic force microscope (Dimension 3100; Veeco, Plainview, NY). The stiffness of the cantilever ($k = 3.18 \text{ N m}^{-1}$) was calibrated using a standard cantilever (CLFC-NOBO; Bruker, Camarillo, CA).⁵⁴ The tip radius of the AFM probe ($R = 25 \text{ nm}$) was measured by an FEI NovaNano 600 scanning electron microscope. All experiments were carried out at room temperature and 16% humidity inside a customized environmental chamber. A constant deflection rate of $1 \mu\text{m s}^{-1}$ was used in all tests.

For a suspended, circular, linear elastic membrane under a central load, the force versus deflection response can be approximated as²

$$F = \pi\sigma_0 h\delta + \frac{Eh}{q^3 a^2} \delta^3 \quad (\text{Equation 1})$$

where F is the applied force, δ is the membrane center deflection, h is the effective thickness of the specimen (see [Supplemental Information Section S8](#)), σ_0 is the pre-stress in the membrane, a is the membrane radius, E is the elastic modulus, and q is a dimensionless constant defined as $q = 1/(1.05 - 0.15\nu - 0.16\nu^2)$, where ν is the Poisson's ratio. According to previous density functional-based tight-binding calculations,^{16,17} the Poisson ratio of the systems studied here was taken as 0.2. We defined specific guidelines to select the fitting region on the raw data (see [Supplemental Information Section S5](#)) to achieve consistency when fitting the linear elastic behavior of different samples.

All-Atom Molecular Dynamics Simulations of GO-PVA Fracture Process

The LAMMPS (large-scale atomic/molecular massively parallel simulator) software package was employed to carry out all-atom MD simulations.⁵⁵ Although it is computationally prohibitive to simulate the experimental indentation and crack initiation, estimates on mechanical properties can be obtained based on mechanistically equivalent systems, as demonstrated in fracture mechanics theory (see below). To this end, two GO sheets with a size of approximately $3 \times 7 \text{ nm}^2$ (70% degree of oxidation and a 4:1 epoxide-to-hydroxyl functional group ratio) were separated with an initial crack opening of 1 nm to mimic a previously initiated crack within an oxidized domain. The GO models were constructed employing a configurational bias Monte Carlo algorithm discussed elsewhere,¹⁶ and the chemical composition of GO was validated by comparing our XPS results with those of previous literature,¹⁷ where an epoxide-rich GO chemistry was reported. Six PVA chains (134 monomers each, $\sim 33 \text{ nm}$ contour length) were deposited over this GO system to simulate GO-PVA nanolaminates. This integer number of PVA chains was chosen to achieve a final PVA single-chain adlayer with a density of 1.06 g cm^{-3} (see further discussion below), as close as possible to the density of bulk PVA ($1.19\text{--}1.31 \text{ g cm}^{-3}$).⁵⁶

The PVA chains were generated employing a random walk algorithm within a box with the same in-plane dimensions as the assembled GO sheets. The resulting PVA layer was pre-equilibrated at 600 K for 4 ns, followed by an annealing process of 1 ns/300 K using the OPLS force field.⁵⁷ During the equilibration, this PVA layer was restricted by repulsive-only potential walls in the out-of-plane-directions of GO to maintain a thickness of $\sim 1 \text{ nm}$ (thickness of a single polymer chain), close to the thickness obtained experimentally (1.5 nm). As mentioned above, the final density of this layer is similar to the bulk density of PVA, ensuring the formation of physically meaningful structures in our simulation that can account for realistic polymer relaxation dynamics while maintaining a single-chain nature for the layer. This equilibrated PVA layer was then deposited over the separated GO sheets to generate the initial structure

for crack-opening simulations. To consider statistical effects, we placed the initial crack at different lateral positions with respect to the deposited PVA layer. To estimate an optimum in crack-bridging behavior, whereby all PVA chains are perpendicular to the crack present in GO and capable of bridging, we also created a directionally biased PVA layer. All models were separately re-equilibrated prior to loading, to permit polymer dynamics in the presence of GO to occur.

The ReaxFF force field,³⁴ as parametrized³⁵ for simulations with hydrocarbons and graphene oxide-based systems, was employed for the crack-opening simulations to describe the interactions between all components. A time step of 0.25 fs was employed to consider the vibrational frequency of H atoms present in PVA and GO. The GO-PVA system was first equilibrated in an NVT ensemble at a temperature of 300 K for 200 ps. The behavior of the system was monitored until energy convergence was achieved during equilibration. The measured out-of-plane thickness of the system was ~ 2 nm after equilibrium, in agreement with experimentally measured thicknesses (~ 2.5 nm). A displacement-controlled uniaxial tensile strain experiment was then performed by deforming the simulation box perpendicular to the initial crack in the system (see Figure 4A) within an NVT ensemble at 300 K. Periodic boundary conditions were applied on the in-plane directions of GO. A strain rate of $1 \times 10^9 \text{ s}^{-1}$ was chosen, as we found this value to be sufficiently low for stable hydrogen-bond reformation to occur. Under this strain rate, shear forces in the interface plateau to an approximately constant value as predicted by Bell's hydrogen-bonding stick-slip mechanisms (see Supplemental Information Section S6 for detailed discussion on the relationship between strain rate and shear force for a variety of strain rates for GO-PVA nanolaminates). Per-atom virial stresses for PVA and GO were independently calculated and summed, and subsequently averaged over 10 timesteps for every 100 timesteps. A forward-moving average filter of 50 steps was then applied to obtain average virial stresses. These average virial stresses (stress \times volume) were then divided by the current box length in the crack-opening direction to calculate the x-component of the bridging force. To calculate 2D traction we divided the bridging force by the crack length, which is also the box width. The crack opening was calculated by measuring the average distance between the atoms involved in the GO crack edges (see Figure 4A).

Quantification of GO-PVA Energy-Release Rate

To verify the failure mechanism and quantify the energy-release rate for GO-PVA, we adapted crack-bridging theory from fracture mechanics²⁰ and contrasted the energy-release rate to that of GO only.¹⁵ Similar to any crack-bridging system, the energy-release rate of GO-PVA nanolaminates was related to the numerical integral of traction with respect to crack opening (shaded region in Figure 4A).

Process Zone Estimation Based on the Extended Finite Elements Method

The extended finite element methodology (XFEM),⁵⁸ as implemented in ABAQUS 6.14, was applied to model the fracture process in GO-PVA by considering the traction-crack-opening behavior of GO and PVA. Plane-stress elements (CPS4) as implemented in ABAQUS 6.14 were utilized, with an element size of 1 nm. To conduct the study, we designed a $60 \times 180 \text{ nm}^2$ GO sheet with a 2-nm-long slit (represented as a strong discontinuity in the XFEM method). Simulations were conducted by incorporating the critical energy-release rate of GO¹⁵ ($G_c = G_0 = 3.4\text{--}4.6 \text{ nJ m}^{-1}$) and the cohesive traction-separation law, as obtained from the all-atom MD simulations previously described. GO was assumed to behave as an isotropic, linear elastic material with Young's modulus $E = 220 \text{ GPa}$ and Poisson's ratio $\nu = 0.2$. The crack-bridging effect of PVA is implicitly implemented into the cohesive law after crack initiation in GO. To

estimate the process zone, we extracted the traction near the crack tip after steady-state crack growth was achieved. The process zone is defined as the distance over which the load is being borne by the PVA traction-crack-opening law (Figure 4B).

Finite Element Analysis of the Membrane-Deflection Experiment

GO and PVA are simulated as two layers using thin-shell elements.⁵⁹ The indenter was modeled as a rigid solid with a tip radius of 25 nm. The cohesion between GO and PVA was simulated as a surface-based (zero-thickness) cohesive law. The parameters for the cohesive law were estimated from a set of MD simulations using ReaxFF (adhesion energy = $0.3425 \text{ nN nm}^{-1}$, shear strength = 93 MPa, and power law [with exponent equal to 1] for mix-mode behavior). The GO constitutive law is based on our prior work.^{16,60} The PVA constitutive law was obtained through an inverse method described in detail in the Supplemental Information Section S9.

SUPPLEMENTAL INFORMATION

Supplemental Information can be found online at <https://doi.org/10.1016/j.matt.2019.04.005>.

ACKNOWLEDGMENTS

The authors acknowledge the support of NSF through DMREF award no. CMMI-1235480, Multi-University Research Initiative (MURI) awards through the Air Force of Scientific Research (AFOSR-FA9550-15-1-0009), and the Army Research Office (W911NF-08-1-0541). Material characterization used the Keck-II facility (NUANCE Center-Northwestern University). Use of the Center for Nanoscale Materials, an Office of Science user facility, was supported by the US Department of Energy, Office of Science, Office of Basic Energy Sciences, under contract no. DE-AC02-06CH11357. The authors thank Dr. Fan Zhou for assistance in the preparation of the Si substrate. R.A.S.-C. acknowledges support from NSF through the Graduate Research Fellowships Program (GRFP), partial support from the Northwestern University Ryan Fellowship, and partial support from Northwestern University through a Royal Cabell Terminal Year Fellowship. H.T.N. acknowledges support from the Vietnam Education Foundation. The authors thank R. Ramachandramoorthy, M. Chon, R. Yang, M. Daly, and D. Restrepo for helpful discussions.

AUTHOR CONTRIBUTIONS

H.D.E., S.T.N., and J.H. designed and supervised the research. H.D.E. guided the experimental and computational mechanics aspects of the project. J.H. and S.T.N. guided material synthesis and polymer modification. R.A.S.-C. and X.W. conducted the mechanical experiments and analyzed the data. L.M. conducted the sample-synthesis and -characterization experiments. J.W. conducted the HRTEM, STEM, and EELS characterization of the samples and analyzed the results. R.A.S.-C. and X.Z. conducted the all-atom MD simulations, and H.T.N. performed the finite-element modeling calculations and crack-bridging analysis in GO-PVA. All authors contributed in writing, reading, and commenting on the manuscript.

DECLARATION OF INTERESTS

The authors declare no competing interests.

Received: January 23, 2019

Revised: March 12, 2019

Accepted: April 15, 2019

Published: May 29, 2019

REFERENCES

- Akinwande, D., Brennan, C.J., Bunch, J.S., Egberts, P., Felts, J.R., Gao, H., Huang, R., Kim, J.-S., Li, T., and Li, Y. (2017). A review on mechanics and mechanical properties of 2D materials—graphene and beyond. *Extreme Mech. Lett.* 13, 42–77.
- Lee, C., Wei, X., Kysar, J.W., and Hone, J. (2008). Measurement of the elastic properties and intrinsic strength of monolayer graphene. *Science* 321, 385–388.
- Gao, C., Daly, M., Chen, B., Howe, J.Y., Singh, C.V., Filletier, T., and Sun, Y. (2015). Strengthening in graphene oxide nanosheets: bridging the gap between interplanar and intraplanar fracture. *Nano Lett.* 15, 6528–6534.
- Cao, C., Daly, M., Singh, C.V., Sun, Y., and Filletier, T. (2015). High strength measurement of monolayer graphene oxide. *Carbon* 81, 497–504.
- Zhang, P., Ma, L., Fan, F., Zeng, Z., Peng, C., Loya, P.E., Liu, Z., Gong, Y., Zhang, J., and Zhang, X. (2014). Fracture toughness of graphene. *Nat. Commun.* 5, 3782.
- Wang, S., Gao, E., and Xu, Z. (2019). Interfacial failure boosts mechanical energy dissipation in carbon nanotube films under ballistic impact. *Carbon* 146, 139–146.
- Wetzel, E.D., Balu, R., and Beaudet, T.D. (2015). A theoretical consideration of the ballistic response of continuous graphene membranes. *J. Mech. Phys. Solids* 82, 23–31.
- Sandoz-Rosado, E., Beaudet, T.D., Andzelm, J.W., and Wetzel, E.D. (2018). High strength films from oriented, hydrogen-bonded “graphamid” 2D polymer molecular ensembles. *Sci. Rep.* 8, 3708.
- Xie, W., Tadepalli, S., Park, S.H., Kazemi-Moridani, A., Jiang, Q., Singamaneni, S., and Lee, J.-H. (2018). Extreme mechanical behavior of nacre-mimetic graphene-oxide and silk nanocomposites. *Nano Lett.* 18, 987–993.
- Zhang, Y., and Li, X. (2017). Bioinspired, graphene/Al₂O₃ doubly reinforced aluminum composites with high strength and toughness. *Nano Lett.* 17, 6907–6915.
- Erickson, K., Erni, R., Lee, Z., Alem, N., Gannett, W., and Zettl, A. (2010). Determination of the local chemical structure of graphene oxide and reduced graphene oxide. *Adv. Mater.* 22, 4467–4472.
- Zhang, T., Li, X., and Gao, H. (2014). Defects controlled wrinkling and topological design in graphene. *J. Mech. Phys. Solids* 67, 2–13.
- Sandoz-Rosado, E., Beaudet, T., Balu, R., and Wetzel, E. (2016). Designing molecular structure to achieve ductile fracture behavior in a stiff and strong 2D polymer, “graphylene”. *Nanoscale* 8, 10947–10955.
- Dreyer, D.R., Park, S., Bielawski, C.W., and Ruoff, R.S. (2010). The chemistry of graphene oxide. *Chem. Soc. Rev.* 39, 228–240.
- Meng, Z., Soler-Crespo, R.A., Xia, W., Gao, W., Ruiz, L., Espinosa, H.D., and Keten, S. (2017). A coarse-grained model for the mechanical behavior of graphene oxide. *Carbon* 117, 476–487.
- Soler-Crespo, R.A., Gao, W., Xiao, P., Wei, X., Paci, J.T., Henkelman, G., and Espinosa, H.D. (2016). Engineering the mechanical properties of monolayer graphene oxide at the atomic level. *J. Phys. Chem. Lett.* 7, 2702–2707.
- Wei, X., Mao, L., Soler-Crespo, R.A., Paci, J.T., Huang, J., Nguyen, S.T., and Espinosa, H.D. (2015). Plasticity and ductility in graphene oxide through a mechanochemically induced damage tolerance mechanism. *Nat. Commun.* 6, 8029.
- Ma, J., Li, Y., Yin, X., Xu, Y., Yue, J., Bao, J., and Zhou, T. (2016). Poly (vinyl alcohol)/graphene oxide nanocomposites prepared by in situ polymerization with enhanced mechanical properties and water vapor barrier properties. *RSC Adv.* 6, 49448–49458.
- Compton, O.C., Cranford, S.W., Putz, K.W., An, Z., Brinson, L.C., Buehler, M.J., and Nguyen, S.T. (2012). Tuning the mechanical properties of graphene oxide paper and its associated polymer nanocomposites by controlling cooperative intersheet hydrogen bonding. *ACS Nano* 6, 2008–2019.
- Bao, G., and Suo, Z. (1992). Remarks on crack-bridging concepts. *Appl. Mech. Rev.* 45, 355–366.
- Budiansky, B., and Amazigo, J.C. (1989). Toughening by aligned, frictionally constrained fibers. *J. Mech. Phys. Solids* 37, 93–109.
- Budiansky, B., Evans, A.G., and Hutchinson, J.W. (1995). Fiber-matrix debonding effects on cracking in aligned fiber ceramic composites. *Int. J. Solids Struct.* 32, 315–328.
- Stannard, A. (2011). Dewetting-mediated pattern formation in nanoparticle assemblies. *J. Phys.: Condens. Matter* 23, 083001.
- Konurr, R., Kargupta, K., and Sharma, A. (2000). Instability and morphology of thin liquid films on chemically heterogeneous substrates. *Phys. Rev. Lett.* 84, 931–934.
- Wan, S., Peng, J., Jiang, L., and Cheng, Q. (2016). Bioinspired graphene-based nanocomposites and their application in flexible energy devices. *Adv. Mater.* 28, 7862–7898.
- Xu, Y., Hong, W., Bai, H., Li, C., and Shi, G. (2009). Strong and ductile poly (vinyl alcohol)/graphene oxide composite films with a layered structure. *Carbon* 47, 3538–3543.
- Abd El-Kader, K.A.M., and Abdel Hamied, S.F. (2002). Preparation of poly (vinyl alcohol) films with promising physical properties in comparison with commercial polyethylene film. *J. Appl. Polym. Sci.* 86, 1219–1226.
- Konidari, M., Papadokostaki, K., and Sanopoulou, M. (2011). Moisture-induced effects on the tensile mechanical properties and glass-transition temperature of poly (vinyl alcohol) films. *J. Appl. Polym. Sci.* 120, 3381–3386.
- Abd El-Kader, K.A.M., Hamied, S.F.A., Mansour, A.B., El-Lawindy, A.M.Y., and El-Tantaway, F. (2002). Effect of the molecular weights on the optical and mechanical properties of poly (vinyl alcohol) films. *Polym. Test* 21, 847–850.
- Beese, A.M., An, Z., Sarkar, S., Nathamgari, S.S.P., Espinosa, H.D., and Nguyen, S.T. (2014). Defect-tolerant nanocomposites through bio-inspired stiffness modulation. *Adv. Funct. Mater.* 24, 2883–2891.
- Putz, K.W., Compton, O.C., Palmeri, M.J., Nguyen, S.T., and Brinson, L.C. (2010). High-nanofiller-content graphene oxide-polymer nanocomposites via vacuum-assisted self-assembly. *Adv. Funct. Mater.* 20, 3322–3329.
- Gong, S., Ni, H., Jiang, L., and Cheng, Q. (2016). Learning from nature: constructing high performance graphene-based nanocomposites. *Mater. Today* 20, 210–219.
- Budiansky, B., Amazigo, J.C., and Evans, A.G. (1988). Small-scale crack bridging and the fracture toughness of particulate-reinforced ceramics. *J. Mech. Phys. Solids* 36, 167–187.
- Van Duin, A.C., Dasgupta, S., Lorient, F., and Goddard, W.A. (2001). ReaxFF: a reactive force field for hydrocarbons. *J. Phys. Chem. A* 105, 9396–9409.
- Huang, L., Seredych, M., Bandoz, T.J., Van Duin, A.C., Lu, X., and Gubbins, K.E. (2013). Controllable atomistic graphene oxide model and its application in hydrogen sulfide removal. *J. Chem. Phys.* 139, 194707.
- Liu, L., Gao, Y., Liu, Q., Kuang, J., Zhou, D., Ju, S., Han, B., and Zhang, Z. (2013). High mechanical performance of layered graphene oxide/poly (vinyl alcohol) nanocomposite films. *Small* 9, 2466–2472.
- Kou, L., and Gao, C. (2013). Bioinspired design and macroscopic assembly of poly (vinyl alcohol)-coated graphene into kilometers-long fibers. *Nanoscale* 5, 4370–4378.
- Barthelat, F., and Espinosa, H. (2007). An experimental investigation of deformation and fracture of nacre—mother of pearl. *Exp. Mech.* 47, 311–324.
- Espinosa, H.D., Juster, A.L., Latourte, F.J., Loh, O.Y., Gregoire, D., and Zavattieri, P.D. (2011). Tablet-level origin of toughening in abalone shells and translation to synthetic composite materials. *Nat. Commun.* 2, 173.
- Tang, H., Barthelat, F., and Espinosa, H. (2007). An elasto-viscoplastic interface model for investigating the constitutive behavior of nacre. *J. Mech. Phys. Solids* 55, 1410–1438.
- Liu, P., Jin, Z., Katsukis, G., Drahushuk, L.W., Shimizu, S., Shih, C.-J., Wetzel, E.D., Taggart-Scarff, J.K., Qing, B., and Van Vliet, K.J. (2016). Layered and scrolled nanocomposites with aligned semi-infinite graphene inclusions at the platelet limit. *Science* 353, 364–367.
- Søndergaard, R.R., Hösel, M., and Krebs, F.C. (2013). Roll-to-roll fabrication of large area functional organic materials. *J. Polym. Sci. B Polym. Phys.* 51, 16–34.
- Mittal, N., Ansari, F., Gowda, V.K., Brouzet, C., Chen, P., Larsson, P.T., Roth, S.V., Lundell, F., Wågberg, L., and Kotov, N.A. (2018). Multiscale control of nanocellulose assembly: transferring

remarkable nanoscale fibril mechanics to macroscale fibers. *ACS Nano* **12**, 6378–6388.

44. Roenbeck, M.R., Furmanchuk, A.o., An, Z., Paci, J.T., Wei, X., Nguyen, S.T., Schatz, G.C., and Espinosa, H.D. (2015). Molecular-level engineering of adhesion in carbon nanomaterial interfaces. *Nano Lett.* **15**, 4504–4516.
45. Wei, X., Naraghi, M., and Espinosa, H.D. (2012). Optimal length scales emerging from shear load transfer in natural materials: application to carbon-based nanocomposite design. *ACS Nano* **6**, 2333–2344.
46. Wei, X., Filleter, T., and Espinosa, H.D. (2015). Statistical shear lag model—unraveling the size effect in hierarchical composites. *Acta Biomater.* **18**, 206–212.
47. Wei, X., Ford, M., Soler-Crespo, R.A., and Espinosa, H.D. (2015). A new Monte Carlo model for predicting the mechanical properties of fiber yarns. *J. Mech. Phys. Solids* **84**, 325–335.
48. Liu, Y., Xie, B., Zhang, Z., Zheng, Q., and Xu, Z. (2012). Mechanical properties of graphene papers. *J. Mech. Phys. Solids* **60**, 591–605.
49. Liu, Y., and Xu, Z. (2014). Multimodal and self-healable interfaces enable strong and tough graphene-derived materials. *J. Mech. Phys. Solids* **70**, 30–41.
50. Weir, M., Johnson, D., Boothroyd, S., Savage, R., Thompson, R., King, S., Rogers, S., Coleman, K., and Clarke, N. (2016). Distortion of chain conformation and reduced entanglement in polymer-graphene oxide nanocomposites. *ACS Macro Lett.* **5**, 430–434.
51. Gao, E., Cao, Y., Liu, Y., and Xu, Z. (2017). Optimizing interfacial cross-linking in graphene-derived materials, which balances intralayer and interlayer load transfer. *ACS Appl. Mater. Interfaces* **9**, 24830–24839.
52. Marcano, D.C., Kosynkin, D.V., Berlin, J.M., Sinitskii, A., Sun, Z., Slesarev, A., Alemany, L.B., Lu, W., and Tour, J.M. (2010). Improved synthesis of graphene oxide. *ACS Nano* **4**, 4806–4814.
53. Cote, L.J., Kim, F., and Huang, J. (2009). Langmuir-Blodgett assembly of graphite oxide single layers. *J. Am. Chem. Soc.* **131**, 1043–1049.
54. Tortorese, M., and Kirk, M. (1997). Characterization of application-specific probes for SPMs. In *Micromachining and Imaging* (International Society for Optics and Photonics), pp. 53–61.
55. Plimpton, S. (1995). Fast parallel algorithms for short-range molecular dynamics. *J. Comput. Phys.* **117**, 1–19.
56. Pritchard, J.G., and Morawetz, H. (1970). *Poly (Vinyl Alcohol): Basic Properties and Uses* (Gordon and Breach Science Publishers).
57. Noorjahan, A., and Choi, P. (2013). Thermodynamic properties of poly (vinyl alcohol) with different tacticities estimated from molecular dynamics simulation. *Polymer* **54**, 4212–4219.
58. Sukumar, N., Chopp, D.L., Moës, N., and Belytschko, T. (2001). Modeling holes and inclusions by level sets in the extended finite-element method. *Comput. Methods Appl. Mech. Eng.* **190**, 6183–6200.
59. DS Simulia Corp. (2014). *Abaqus v.14 Documentation* (Dassault Systemes Simulia Corporation). <http://ivt-abaqusdoc.ivt.ntnu.no:2080/v6.14/index.html>.
60. Benedetti, I., Nguyen, H., Soler-Crespo, R.A., Gao, W., Mao, L., Ghasemi, A., Wen, J., Nguyen, S., and Espinosa, H.D. (2018). Formulation and validation of a reduced order model of 2D materials exhibiting a two-phase microstructure as applied to graphene oxide. *J. Mech. Phys. Solids* **112**, 66–88.